Chemical Engineering Journal 155 (2009) 223–233

Contents lists available at ScienceDirect

Chemical Engineering Journal

journal homepage: www.elsevier.com/locate/cej

Photocatalytic activity of nanocrystalline mesoporous-assembled TiO_2 photocatalyst for degradation of methyl orange monoazo dye in aqueous wastewater

Piyanud Jantawasu [a], Thammanoon Sreethawong [a,b,*], Sumaeth Chavadej [a,b]

[a] The Petroleum and Petrochemical College, Chulalongkorn University, Soi Chula 12, Phyathai Road, Pathumwan, Bangkok 10330, Thailand
[b] Center for Petroleum, Petrochemicals, and Advanced Materials, Chulalongkorn University, Bangkok 10330, Thailand

ARTICLE INFO

Article history:
Received 2 December 2008
Received in revised form 1 March 2009
Accepted 17 July 2009

Keywords:
Titania
Mesoporous assembly
Decolorization
Degradation
Methyl orange

ABSTRACT

In this work, nanocrystalline mesoporous-assembled TiO_2 photocatalyst was synthesized by a sol–gel process with the aid of a structure-directing surfactant and employed for the photocatalytic degradation of methyl orange azo dye (monoazo dye), as compared to various commercially available non-mesoporous-assembled TiO_2 powders. The experimental results showed that the synthesized mesoporous-assembled TiO_2 nanocrystal calcined at 500 °C provided superior decolorization and degradation performance to the non-mesoporous-assembled commercial TiO_2 powders. In addition, several operational parameters affecting the decolorization and degradation of methyl orange, namely photocatalyst dosage, initial dye concentration, H_2O_2 concentration, and initial solution pH, were systematically investigated, using the mesoporous-assembled TiO_2 nanocrystal. The optimum conditions were a photocatalyst dosage of 7 g/l, an initial dye concentration of 5 mg/l, a H_2O_2 concentration of 0.5 M, and an initial solution pH of 4.7, exhibiting the highest decolorization rate of methyl orange.

1. Introduction

Azo compounds are an important class of synthetic dyes and represent the largest class of dyes applied in textile processing. They are ordinarily characterized by the presence of one or more azo groups (–N=N–) bound to aromatic rings [1,2]. Methyl orange (MO) or acid orange 52 (AO 52) is an azo compound, which is commonly used as a coloring agent in several applications, such as textile, paint, ink, plastic, and cosmetic industries. The release of this coloring agent present in wastewater definitely causes a severe environmental problem [3–5]. Several techniques have been developed to treat wastewaters containing the dye pollutants. Up to now, many conventional methods, including physical methods (such as adsorption), biological methods, chemical methods (such as chlorination and ozonation), and their combinations, have been widely studied and used for treating the dye-containing wastewaters [1,6–10]. The conventional processes for treating these effluents are insufficient to purify the wastewaters because the disadvantage of these methods is the incomplete destruction of the pollutant compounds, as they just transfer the compounds present from aqueous to another phase, thus causing secondary pollution problem. Consequently, the post-treatment of generated sludges and the regeneration of adsorbent materials, which are comparatively expensive operations, are required [11,12].

Photocatalysis, one of advanced oxidation processes (AOPs), is an efficient technique for water and air purification due to its several advantages [3,4,12–15]. Firstly, it destroys the pollutants by decomposing or transforming into less harmful substances in the presence of UV or near-UV illumination. Secondly, several non-toxic materials can be used as a semiconductor photocatalyst, particularly titanium dioxide (TiO_2). Thirdly, this process can be operated at atmospheric pressure and near or slightly higher than room temperature. Finally, the photocatalytic processes can provide a low operating cost due to the use of sunlight as the source of irradiation, also implying as an environmental cleaning process. So far, the TiO_2-composed photocatalytic systems have become emerging technology for destroying the organic dye pollutants because the TiO_2 photocatalysts are largely available, inexpensive, and non-toxic, and show relatively high chemical stability. The primary photocatalytic processes occur upon the irradiation of light with energy greater than or equal to the band gap of the TiO_2 photocatalyst. Under the light irradiation, the electrons (transferring to the conduction band, CB) and holes (remaining at the valence band, VB) are then generated and trapped on the photocatalyst surface, subsequently producing reactive oxygen species, such as $OH^{\bullet}$ and $O_2^{\bullet -}$ radicals, to decompose the organic dye pollutants. The mechanisms

* Corresponding author at: The Petroleum and Petrochemical College, Chulalongkorn University, Soi Chula 12, Phyathai Road, Pathumwan, Bangkok 10330, Thailand. Tel.: +66 2 218 4144; fax: +66 2 215 4459.
E-mail address: thammanoon.s@chula.ac.th (T. Sreethawong).

1385-8947/$ – see front matter © 2009 Elsevier B.V. All rights reserved.
doi:10.1016/j.cej.2009.07.036

for the heterogeneous photocatalytic degradation of dyes have been investigated and proposed by several research groups [16–18].

Various approaches, such as hydrothermal method, solvothermal method, sol–gel method, spray pyrolysis method, supercritical carbon dioxide method, and electrospinning method, have been developed to synthesize the TiO_2 photocatalysts as advanced materials with specific functions [19–24]. Some conventional processes for synthesizing TiO_2 photocatalysts, such as hydrothermal method, inevitably face with many disadvantages: for example, inhomogeneous crystal particles having a relative large size are normally obtained, and this method is quite costly [25]. However, there are many factors that affect the photocatalytic activity of the photocatalysts, such as composition homogeneity, crystal size and structure, specific surface area, morphology (shape and size), as well as porosity and pore size distribution [26].

Several works reported the use of various methods for synthesizing mesoporous-structured TiO_2 photocatalysts [27–38]. However, to our knowledge, the preparation of a mesoporous-assembled TiO_2 nanocrystal photocatalyst by using a sol–gel process with the aid of the structure-directing surfactant, as well as its application in wastewater treatment, has not yet been extensively investigated. The mesoporous-assembled TiO_2 nanocrystal is very promising to be used for the photocatalytic degradation of the azo dye because it possesses very small physical dimensions: a large pore volume for reactant accessibility, a uniform pore size distribution, and a high volume fraction of atom located at the surface, which are very useful for this application.

In our previous works [39–42], the nanocrystalline mesoporous-assembled TiO_2 photocatalyst was synthesized by such the method without and with metal loadings. Therefore, in this present work, by following the previous works' accomplishment, the experimental investigation was performed on the photocatalytic degradation of MO, a model monoazo dye present in wastewaters from the textile industry, using the mesoporous-assembled TiO_2 nanocrystal as compared to various commercially available non-mesoporous-assembled TiO_2 powders. Various synthetic and reaction parameters, such as calcination condition for the photocatalyst preparation, photocatalyst dosage, initial dye concentration, hydrogen peroxide (oxidant) concentration, and initial solution pH, were carefully studied on the photocatalytic performance for MO decolorization and degradation (as degradation in overall).

2. Experimental

2.1. Materials

Tetraisopropyl orthotitanate (TIPT, $Ti(OCH(CH_3)_2)_4$, Merck Co., Ltd.), laurylamine hydrochloride (LAHC, $CH_3(CH_2)_{11}NH_2{\cdot}HCl$, Merck Co., Ltd.), acetylacetone (ACA, $CH_3COCH_2COCH_3$, Carlo Erba Reagents Co., Ltd.), methyl orange (MO, $C_{14}H_{14}N_3O_3SNa$, Nacalai Tesque), hydrochloric acid (37% HCl, Lab Scan Co., Ltd.), and hydrogen peroxide (30% H_2O_2, Carlo Erba Reagents Co., Ltd.) were used in this study. All chemicals were of analytical grade and used without further purification. The TIPT was used as a titanium precursor for synthesizing the mesoporous-assembled TiO_2 photocatalyst. The LAHC was used as a structure-directing surfactant behaving as a mesopore-forming agent. It is worth noting that without the LAHC, gelation could not occur, indicating that the LAHC also behaved as a gel formation-assisting agent. The ACA, which acts as a modifying ligand, was applied to moderate the hydrolysis and condensation processes of the titanium precursor. Commercially available TiO_2 powders, P-25 TiO_2 (J.J. Degussa Hüls Co., Ltd.), which is well-known to possess very high photocatalytic activity, ST-01 TiO_2 (Ishihara Sangyo Co., Ltd.), and JRC-03 TiO_2 (Ishihara Sangyo Co., Ltd.), were selected for the comparative studies of the photocatalytic MO degradation.

2.2. Photocatalyst synthesis procedure

The nanocrystalline mesoporous-assembled TiO_2 photocatalyst was synthesized via a sol–gel process with the aid of a structure-directing surfactant in a system consisting of LAHC and ACA-modified TIPT [39]. A specified amount of ACA was first introduced into the TIPT with the molar ratio of unity. The mixed solution was then gently shaken until intimate mixing. Afterwards, a 0.1 M LAHC aqueous solution with a pH of 4.2 was added to the ACA-modified TIPT solution, in which the molar ratio of TIPT to LAHC was adjusted to a value of 4:1. The mixture was kept continuously stirring at 40 °C overnight to obtain a transparent yellow sol. Then, the gel was completely formed by placing the TiO_2 sol into an oven at 80 °C for a week. Accordingly, the gel was dried overnight at 80 °C to eliminate the solvent, which was mainly distilled water used for preparation of the LAHC aqueous solution. The dried sample was then calcined at different temperatures in the range of 500–700 °C for 4 h to remove the LAHC surfactant, and subsequently the desired mesoporous-assembled TiO_2 photocatalyst was achieved.

2.3. Characterization techniques

The N_2 adsorption–desorption isotherms of all the photocatalysts were obtained by using a nitrogen adsorption–desorption apparatus (Quantachrome, Autosorb-1) at a liquid nitrogen temperature of −196 °C. The Brunauer–Emmett–Teller (BET) approach using adsorption data over the relative pressure ranging from 0.05 to 0.35 was utilized to determine the specific surface areas of the photocatalysts. The Barrett–Joyner–Halenda (BJH) approach was used to determine the mean pore size and pore size distribution of the photocatalyst samples. The sample was degassed at 150 °C for 2 h to remove any physisorbed gases prior to the measurement. X-ray diffraction (XRD) was used to identify the structure and the composition of all the crystalline TiO_2 photocatalysts. A Rigaku PMG-A2 XRD system generating monochromated Cu K_α radiation with a continuous scanning mode at the rate of 2°/min and operating conditions of 40 kV and 30 mA was used to obtain the XRD patterns. Crystallite size (D) of the photocatalysts was calculated from the line broadening of X-ray diffraction peak according to the Sherrer formula [43], as shown in Eq. (1):

$$D = \frac{K\lambda}{\beta\ \cos(\theta)} \tag{1}$$

where K is the Sherrer constant (0.89), λ is the wavelength of the X-ray radiation (0.15418 nm for Cu K_α), β is the full width at half maximum (FWHM) of the diffraction peak measured at 2θ, and θ is the diffraction angle. It is well-known that the photocatalytic activity of a photocatalyst is directly related to its band gap energy (E_g). Thus, the UV–vis spectra of the synthesized mesoporous-assembled TiO_2 and the commercial TiO_2 (P-25 TiO_2, ST-01 TiO_2, and JRC-03 TiO_2) were obtained by using a UV–vis spectrophotometer (Shimadzu, UV-2550) in the wavelength range of 250–500 nm at room temperature with $BaSO_4$ as the reference. Afterwards, the absorbance spectra were analyzed to estimate the band gap energy (E_g, eV). The band gap wavelength (λ_g, nm) was the crossing point between the line extrapolated from the onset of the rising part and x-axis of the plot of absorbance as a function of wavelength (λ, nm). The E_g was then determined by using Eq. (2) [39]:

$$E_g = \frac{1240}{\lambda_g} \tag{2}$$

The sample morphology was observed by using a scanning electron microscope (JOEL JSM-6400) and a transmission electron microscope (JEOL 2000 CX) operated at 15 and 200 kV, respectively.

Table 1
Summary of textural properties obtained from N_2 adsorption-desorption results of the synthesized mesoporous-assembled TiO_2 and commercial TiO_2 photocatalysts.

Photocatalyst	Calcination temperature (°C)	Calcination time (h)	BET surface area ($m^2\ g^{-1}$)	Mean pore diameter (nm)	Total pore volume ($cm^3\ g^{-1}$)
Mesoporous-assembled TiO_2	500	4	84.3	6.18	0.158
	600	4	22.7	8.83	0.061
	700	4	9.0	–[a]	–[a]
P-25 TiO_2	–	–	65.0	–[a]	–[a]
ST-01 TiO_2	–	–	289.5	–[a]	–[a]
JRC-03 TiO_2	–	–	55.0	–[a]	–[a]

[a] N_2 adsorption–desorption isotherms correspond to IUPAC type II pattern.

2.4. Photocatalytic activity testing

The photocatalytic activity of the synthesized mesoporous-assembled TiO_2 photocatalysts and the commercial TiO_2 samples (P-25 TiO_2, ST-01 TiO_2, and JRC-03 TiO_2) were investigated using the photodegradation of MO in aqueous solution under UV irradiation (11 W low-pressure mercury lamp, Philips). A desired amount of any tested photocatalysts (synthesized mesoporous-assembled TiO_2 or commercial TiO_2) with various dosages was suspended in a MO solution with various concentrations by using a magnetic stirrer, and the suspension was photoirradiated by the light source. A sample was periodically withdrawn from the reactor for every hour, and the sample was then centrifuged to separate the photocatalyst powder from the solution. The obtained filtrate was taken for an analysis of MO concentration by the absorbance measurement. The absorbance of the solution samples was monitored by the UV–vis spectrophotometer in the wavelength range of 200–800 nm and was used to determine the percentage of MO degradation. The TOC analysis of the solution samples obtained under the optimum conditions was also performed by using a TOC analyzer (Shimadzu, TOC-5000A).

Moreover, the pseudo-first-order rate constant (k, h^{-1}) for both the photocatalytic decolorization and degradation (as degradation in overall) of MO was determined by Eq. (3) [12,44–46]:

$$\ln\left(\frac{C_0}{C}\right) = kt \tag{3}$$

The k value was calculated from the plot between $\ln(C_0/C)$ and time (t), where C_0 and C denote the MO concentrations at $t = 0$ and $t = t$, respectively. The pseudo-first-order rate constant was used as the indicator for evaluating the photocatalytic activity of the synthesized mesoporous-assembled TiO_2 photocatalyst, as compared to the commercial TiO_2 photocatalysts (P-25 TiO_2, ST-01 TiO_2, and JRC-03 TiO_2).

3. Results and discussion

3.1. Characterization results of photocatalysts

The physicochemical properties of the nanocrystalline mesoporous-assembled TiO_2 photocatalysts synthesized by the sol–gel process with the aid of a structure-directing surfactant could be influenced by many factors, especially calcination temperature. In this work, the synthesized mesoporous-assembled TiO_2 calcined at various temperatures was investigated, as compared to various types of commercial TiO_2, namely P-25 TiO_2, ST-01 TiO_2, and JRC-03 TiO_2.

3.1.1. N_2 adsorption–desorption results

In order to verify the mesoporosity of the photocatalyst samples, the N_2 adsorption–desorption analysis is very powerful technique normally used. The N_2 adsorption–desorption isotherms of the synthesized TiO_2 calcined at 500 and 600 °C exhibits typical IUPAC type IV pattern [47], as shown in Fig. 1(a) and (b), respectively. The hysteresis loop is ascribed to the existence of mesoporous structure (mesopore size between 2 and 50 nm) in the obtained products. A sharp increase in adsorption volume of N_2 was observed and located in the P/P_0 range of 0.5–0.9. This sharp increase can be assigned to the capillary condensation, indicating the good homogeneity of the samples and fairly small pore size since the P/P_0 position of the inflection point is directly related to pore dimension. As illustrated in the insets of Fig. 1(a) and (b), the pore size distribution obtained from this modified sol–gel process at two calcination temperatures is quite narrow, implying the good quality of the samples.

For the commercial TiO_2 samples (P-25 TiO_2, ST-01 TiO_2, and JRC-03 TiO_2), the N_2 adsorption–desorption isotherms correspond to IUPAC type II pattern [47], as depicted in Fig. 2(a), (b), and (c), respectively. It is clear that all the commercial TiO_2 photocatalysts exhibit non-mesoporous characteristics due to the absence of dominant hysteresis loop and the adsorption plateau at a high relative pressure. No capillary condensation of N_2 into the pore was observed since the desorption isotherm was insignificantly different from the adsorption one. The pore size distributions of all the

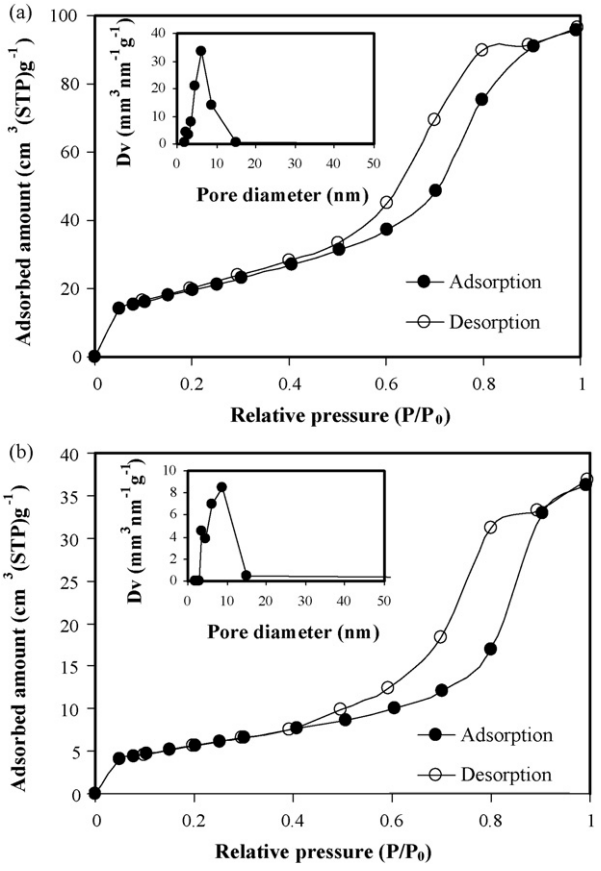

Fig. 1. N_2 adsorption–desorption isotherms of the synthesized mesoporous-assembled TiO_2 calcined at (a) 500 °C and (b) 600 °C (Inset: pore size distribution).

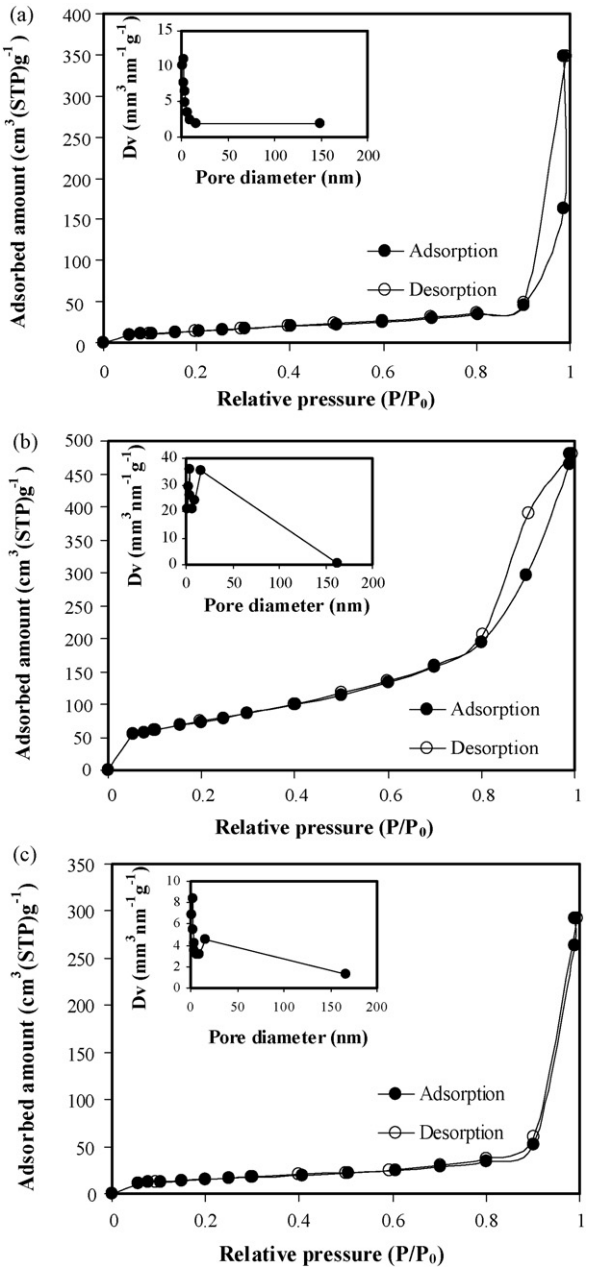

Fig. 2. N_2 adsorption–desorption isotherms of (a) the commercial P-25 TiO_2, (b) the commercial ST-01 TiO_2, and (c) the commercial JRC-03 TiO_2 (Inset: pore size distribution).

commercial TiO_2 photocatalysts, as shown in the insets of Fig. 2(a), (b), and (c), are quite broad. These results show that the average pore sizes of the commercial TiO_2 are quite large since their pore size distributions not only exist in the mesopore region (mesopore size between 2 and 50 nm) but also mostly cover the macropore region (macropore size > 50 nm).

The textural properties of all the investigated photocatalysts, including BET surface area, mean pore diameter, and total pore volume, are summarized in Table 1. For the synthesized mesoporous-assembled TiO_2 photocatalysts, the increase in calcination temperature caused the decreases in surface area and total pore volume and the increase in mean pore diameter, as expected. For the commercial TiO_2 photocatalysts, whose isotherms exhibit IUPAC type II pattern, the mean pore diameter and total pore volume are always not reported because they contain a large portion of macropore, which possesses very broad pore size distribution with the pore diameters larger than 50 nm, up to 200 nm. Therefore, the surface areas of the P-25 TiO_2 and the JRC-03 TiO_2 are consequently observed to be lower than the synthesized mesoporous-assembled TiO_2 calcined at 500 °C, as shown in Table 1. However, the surface area of the ST-01 TiO_2 was observed to be higher than that of the synthesized mesoporous-assembled TiO_2, plausibly resulting from its unique production process.

3.1.2. X-ray diffraction results

The XRD patterns of the synthesized mesoporous-assembled TiO_2 calcined at different temperatures, as compared to the commercial TiO_2 photocatalysts, are shown in Fig. 3. Table 2 also summarizes the XRD results, including crystalline phase, rutile ratio, and crystallite size. The XRD pattern of the synthesized mesoporous-assembled TiO_2 sample calcined at 500 °C shows crystalline structure of the pure anatase phase. The dominant peaks at 2θ about 25.2°, 37.9°, 47.8°, 53.8°, and 55.0°, which represent the indices of (1 0 1), (0 0 4), (2 0 0), (1 0 5), and (2 1 1) planes (JCPDS Card No. 21-1272) [48], respectively, are conformed to the crystalline structure of the anatase TiO_2. However, at the calcination temperature of 500 °C, the crystallization to the anatase phase of the synthesized photocatalyst is not fully developed in a comparison to the calcination temperature of 600 °C, of which the peak intensity of the anatase phase greatly increases. The calcination temperature of 600 °C is not only determined as the highest limit for yielding the well-crystalline pure anatase phase but also as the starting point of phase transformation from the anatase to the rutile phase since an approximately 5% rutile content was observed (Table 2). At the calcination temperature of 700 °C, partial phase transformation from the anatase to the rutile was observed, resulting in the combination of the anatase to the rutile phases with an approximately 79% rutile content (Table 2). The occurrence of the dominant peaks at 2θ about 27.4°, 36.1°, 41.2°, and 54.3°, which correspond to the indices of (1 1 0), (1 0 1), (1 1 1), and (2 1 1) planes (JCPDS Card No. 21-1276) [48], respectively, indicates the presence of the rutile phase in the mesoporous-assembled TiO_2 calcined at this temperature. The main difference between the synthesized mesoporous-assembled TiO_2 and the commercial P-25 TiO_2 photocatalysts was that the commercial P-25 TiO_2 possesses mixed phase of the anatase (74%) and the rutile (26%), of which the phase com-

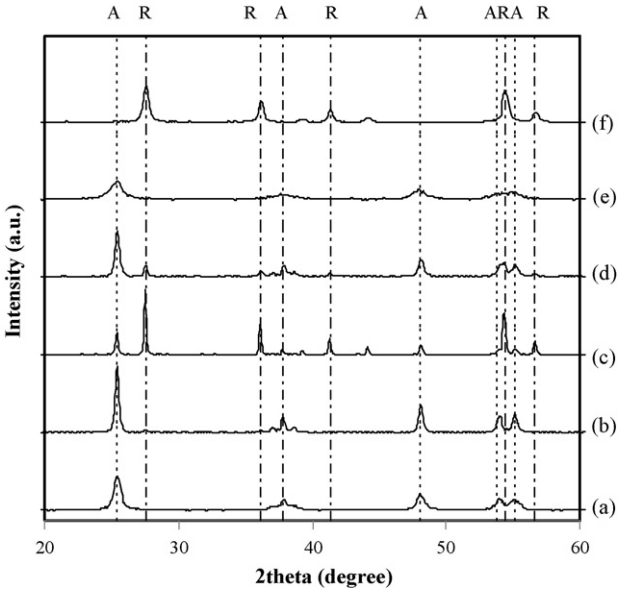

Fig. 3. XRD patterns of synthesized mesoporous-assembled TiO_2 calcined at (a) 500 °C, (b) 600 °C, and (c) 700 °C, as compared to the commercial TiO_2 (d) P-25, (e) ST-01, and (f) JRC-03 (A = Anatase, R = Rutile).

Table 2
Summary of XRD analysis of the synthesized mesoporous-assembled TiO_2 calcined at different temperatures and commercial TiO_2.

Photocatalyst	Calcination temperature (°C)	Calcination time (h)	Phase from XRD pattern	Percentage of rutile (W_R)	Crystallite size (nm)	
					Anatase (1 0 1)	Rutile (1 1 0)
Mesoporous-assembled TiO_2	500	4	Anatase	0	13.64	-
	600	4	Anatase + rutile	5	25.75	46.26
	700	4	Anatase + rutile	79	38.75	53.96
P-25 TiO_2	–	–	Anatase + rutile	26	22.01	28.90
ST-01 TiO_2	–	–	Anatase	0	8.33	–
JRC-03 TiO_2	–	–	Rutile	100	–	17.11

position was calculated by Eqs. (4) and (5) [49], whereas the ST-01 TiO_2 and the JRC-03 TiO_2 possess pure crystalline structure of the anatase and the rutile phase, respectively:

$$W_R = \left[1 + \frac{0.8 I_A}{I_R}\right]^{-1} \quad (4)$$

$$W_A = 1 - W_R \quad (5)$$

where I_A and I_R represent integrated intensities of the anatase (1 0 1) and the rutile (1 1 0) diffraction peaks, respectively, and W_A and W_R represent phase compositions of the anatase and the rutile, respectively.

3.1.3. Band gap energy results

UV–vis spectroscopy was used to investigate the light absorption capability and the band gap energy of the photocatalysts. The UV–vis spectra of the synthesized mesoporous-assembled TiO_2 photocatalyst calcined at different temperatures and the commercial TiO_2 photocatalysts are shown comparatively in Fig. 4. The corresponding absorption wavelength and band gap energy are also summarized in Table 3. From Fig. 4, the absorption bands of all the TiO_2 photocatalysts are approximately in the range of 200–400 nm. The strong absorption band at low wavelength in the spectra indicates the presence of Ti species as the tetrahedral Ti^{4+}. This absorption band is generally associated with the electronic excitation of the valence band O2p electron to the conduction band Ti3d level [50]. The absorption onset is approximately at 387 nm for the synthesized mesoporous-assembled TiO_2 calcined at 500 °C, which corresponds to the band gap energy of the anatase TiO_2 of 3.2 eV. For the synthesized mesoporous-assembled TiO_2 calcined at 600 °C, the absorption band shifts to a higher wavelength of 390 nm, which is correlated to the band gap energy of the mixed anatase and rutile TiO_2 between 3.0 and 3.2 eV, whereas the absorption band of the synthesized mesoporous-assembled TiO_2 calcined at 700 °C further shifts to a wavelength longer than 400 nm, which is closely correlated to the band gap energy of the rutile TiO_2 of 3.02 eV (absorption wavelength of 410 nm). For the commercial TiO_2 photocatalysts, their band gap energy values reported in Table 3 also well correspond to their crystalline phase obtained from the XRD analysis (Fig. 3). As comparatively seen from Fig. 4, it is also perceptible that the light absorption capability of the anatase TiO_2 at near UV region is significantly higher than that of the rutile TiO_2.

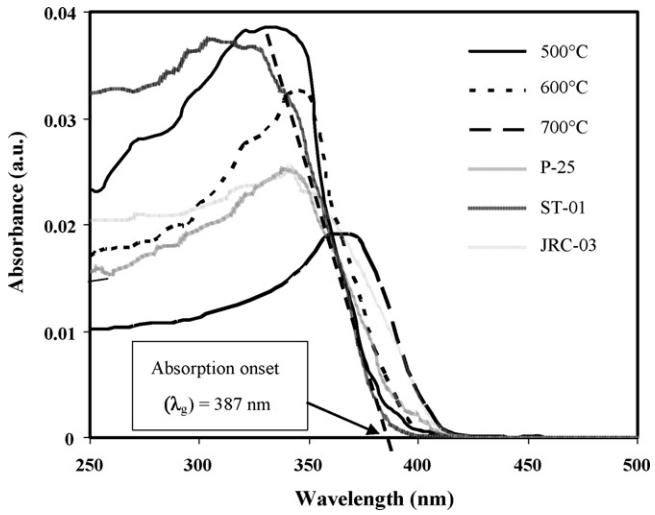

Fig. 4. UV–vis spectra of synthesized mesoporous-assembled TiO_2 photocatalysts calcined at (a) 500 °C, (b) 600 °C, and (c) 700 °C for 4 h and commercial TiO_2 photocatalysts (d) P-25 TiO_2, (e) ST-01 TiO_2, and (f) JRC-03 TiO_2.

3.1.4. SEM and TEM images

Typical SEM and TEM images (for both low and high magnifications) of the investigated photocatalysts are shown in Figs. 5–7, respectively. From the SEM images, the synthesized mesoporous-assembled TiO_2 possesses reasonably uniform size with nanoagglomeration of many crystallites. In addition, the TEM images of the synthesized mesoporous-assembled TiO_2 reveal the formation of highly crystalline TiO_2 aggregates composed of three-dimensional disordered primary nanoparticles. The average size of the mesoporous-assembled TiO_2 nanoparticle calcined at 500 °C is approximately 10–15 nm, which is consistent with the crystallite size estimated from the XRD analysis. Therefore, each particle observed by the TEM analysis could be considered as a single crystal. For the commercial TiO_2 photocatalysts, SEM images also show the agglomeration of many particles; however, the segregation of the agglomerated particles seems to be quite evident than the mesoporous-assembled TiO_2, resulting in the presence of significant content of macropore, as determined by the pore size distribution analysis. Moreover, the particle sizes of all the commercial TiO_2 observed by the TEM analysis agree well with the crystallite sizes calculated from their XRD patterns.

3.2. Photocatalytic MO degradation results

The UV–vis spectrum of a MO solution shows two absorption maxima, as shown in Fig. 8, with the first band centered at 270 nm and the second band at 465 nm. The absorbance at 465 nm is due to the $\pi \rightarrow \pi^*$ transition of the azo group (–N=N–), representing the color of dye solution, and its decrease was used to monitor the decolorization of the MO dye. The other absorbance at 270 nm is due to the $\pi \rightarrow \pi^*$ transition in the aromatic ring, representing

Table 3
Summary of band gap energy obtained from UV-Vis spectra of the photocatalysts.

Photocatalyst	Calcination temperature (°C)	Absorption wavelength, λ_g (nm)	Band gap energy (eV)
Mesoporous-assembled TiO_2	500	387	3.20
	600	390	3.18
	700	405	3.06
P-25 TiO_2	–	395	3.14
ST-01 TiO_2	–	385	3.22
JRC-03 TiO_2	–	410	3.02

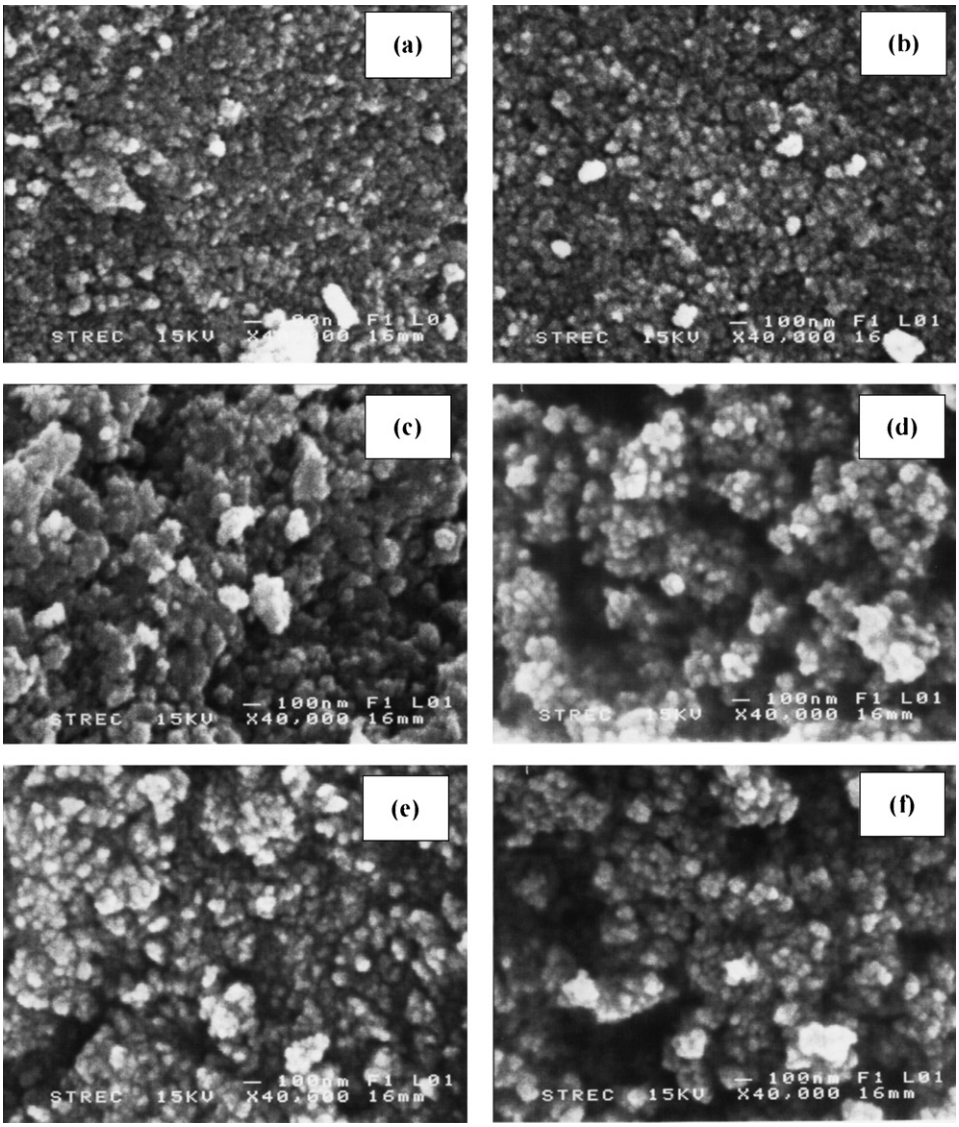

Fig. 5. SEM images of synthesized mesoporous-assembled TiO_2 calcined at (a) 500 °C, (b) 600 °C, (c) 700 °C, and commercial TiO_2 (d) P-25 TiO_2, (e) ST-01 TiO_2, and (f) JRC-03 TiO_2.

the aromatic content of the methyl orange, and its decrease was used to monitor the degradation of aromatic part of the MO dye. Selvam et al. [51] also explained about the photocatalytic decolorization and degradation of a reactive azo dye, Reactive Orange 4 (RO4), of which two corresponding absorption maxima occur at 489 and 285 nm, respectively. Therefore, in this work, both the decolorization and degradation (referred as degradation in overall) of the MO dye in terms of relative concentration (C/C_0) and reaction rate constant were investigated. In addition, Hachem et al. [52] pointed out that the adsorption of RO4 on the commercial TiO_2 photocatalyst was quite fast, and the adsorption/desorption equilibrium could be reached within about 45 min. In this work, the adsorption/desorption equilibrium of the photocatalyst/MO solution suspensions was established by being magnetically stirred in a dark environment for 1 h before starting the reaction experiments.

3.2.1. *Effect of photocatalyst type*

In this work, two main types of the photocatalysts used for studying the photocatalytic degradation of MO were the synthesized mesoporous-assembled TiO_2 calcined at 500, 600, and 700 °C and the non-mesoporous-assembled commercial TiO_2 (P-25 TiO_2, ST-01 TiO_2, and JRC-03 TiO_2). It must be first noted that no appreciable MO degradation was detected in the absence of either light irradiation or photocatalyst. The results of the photocatalytic decolorization and degradation of MO over various types of the TiO_2 photocatalysts are shown in Fig. 9(a) and (b), respectively. The results show that the synthesized mesoporous-assembled TiO_2 calcined at 500 °C gave the highest efficiency for both the decolorization and degradation due to the most rapid decrease in the azo and aromatic concentrations, respectively. The photocatalytic degradation of MO solution is proved to be the pseudo-first-order reaction, and its kinetics can be expressed as $\ln(C_0/C) = kt$. The calculated reaction rate constants (k) of each type of the photocatalyst from Fig. 9(a) and (b) are given in Table 4.

As shown in Table 4, the rate constants of the synthesized mesoporous-assembled TiO_2 for both the decolorization and the degradation decreased with increasing calcination temperature. This might be because of the observed loss in surface area of the photocatalyst, shown in Table 1, which is attributable to the pore coalescence due to the crystallization of walls separating mesopores, as previously explained. Consequently, this tendency caused lower surface active reaction sites and higher probability of a mutual e^-/h^+ recombination, leading to lowering the photocatalytic activity. Moreover, it can be noticed that the increasing rutile

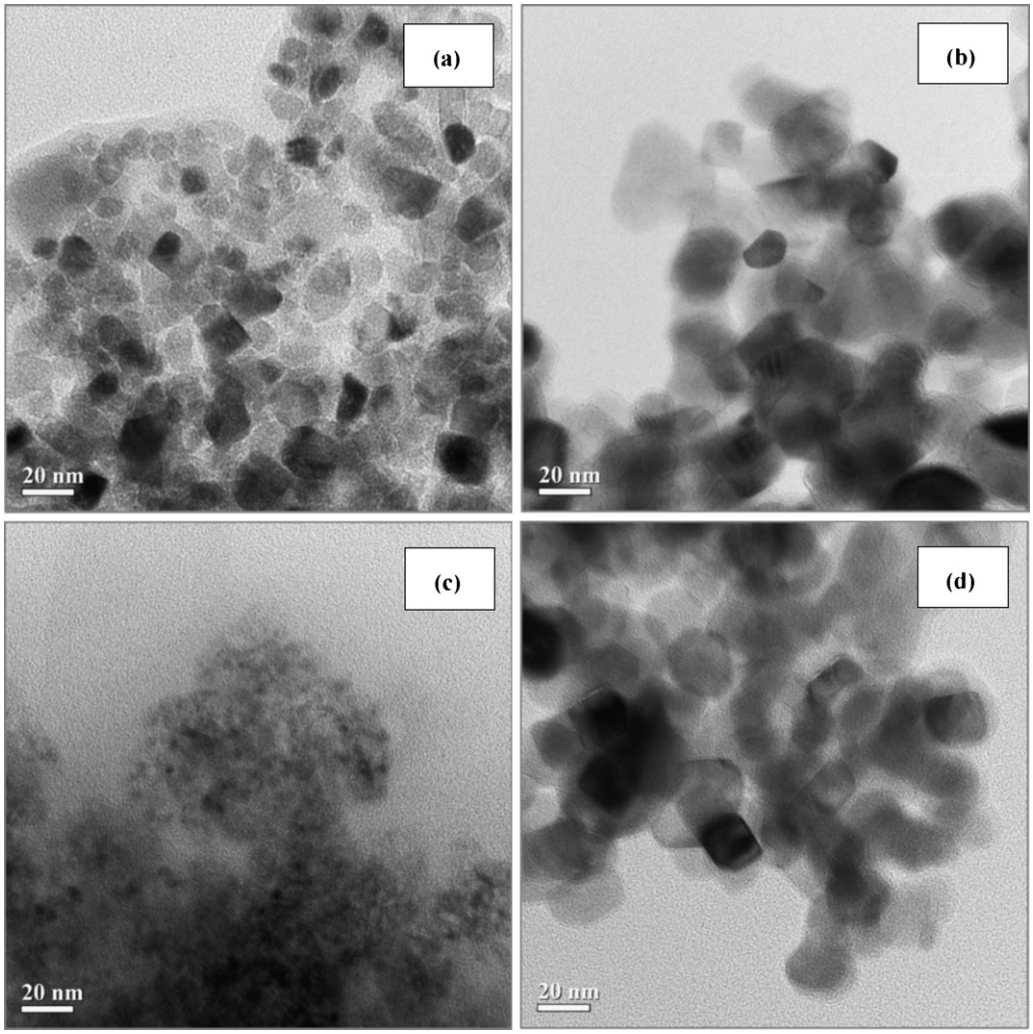

Fig. 6. Low magnification TEM images of (a) synthesized mesoporous-assembled TiO_2 calcined at 500 °C, and commercial TiO_2 (b) P-25 TiO_2 (c) ST-01 TiO_2, and (d) JRC-03 TiO_2.

content in the synthesized TiO_2 photocatalyst calcined at higher temperatures negatively affected the photocatalytic degradation of MO, probably due to the lower flat band level of the rutile than the anatase phase (lower band gap energy).

For P-25 TiO_2, the phase combination between the anatase and the rutile (a rutile ratio of 0.26, as shown in Table 2) and a lower BET surface area than that of the synthesized mesoporous-assembled TiO_2 calcined at 500 °C might be the causes of very low photocatalytic activity. Despite the large surface area about 290 $m^2\ g^{-1}$ of the ST-01 TiO_2, its imperfect crystallization from the XRD pattern (Fig. 3) accompanying with the fairly small crystallite size (Table 2) is considered to increase the probability of the mutual e^-/h^+ recombination at both surface and bulk traps. In the case of the JRC-03 TiO_2, it possesses only the rutile TiO_2 phase, therefore giving the lowest reaction rate. Moreover, the lack of the mesoporous-assembled structure in these three commercial TiO_2 powders (as shown in Figs. 2 and 5) is subjected to have less reactant accessibility for the photocatalytic reaction. In contrast, the use of the nanocrystalline mesoporous-assembled TiO_2 with a uniform pore size and a high crystallinity could decrease the number of lattice defects and then facilitate the electron and hole transport for reacting with water and/or oxygen molecules adsorbed at the TiO_2 surface along the mesoporous structure to create many active species, such as $OH^\bullet$ and $O_2^{\bullet -}$. From the results of the present study, the mesoporosity has been proved to be very important property of the TiO_2 photocatalyst.

Table 4
Comparison of effect of photocatalyst type on the reaction rate constants for both decolorization and degradation of MO by the synthesized mesoporous-assembled TiO_2 photocatalysts calcined at various temperatures and commercial TiO_2 photocatalyst (photocatalyst dosage = 2 g/l; initial MO concentration = 5 mg/l; reaction volume = 80 ml; irradiation time = 4 h).

Photocatalyst	Calcination temperature (°C)	Reaction rate constant, k (h^{-1})	
		Decolorization	Degradation
Mesoporous-assembled TiO_2	500	0.615	0.362
	600	0.405	0.163
	700	0.029	0.019
P-25 TiO_2	–	0.394	0.117
ST-01 TiO_2	–	0.352	0.162
JRC-03 TiO_2	–	0.068	0.050

3.2.2. Effect of photocatalyst dosage

The reaction rate constants for the photocatalytic decolorization and degradation of MO at various dosages of the synthesized mesoporous-assembled TiO_2 photocatalyst calcined at 500 °C, exhibiting the best photocatalytic activity among all the investigated TiO_2 photocatalysts, are shown in Fig. 10. The results indicate that the significant increases in the photocatalytic decolorization

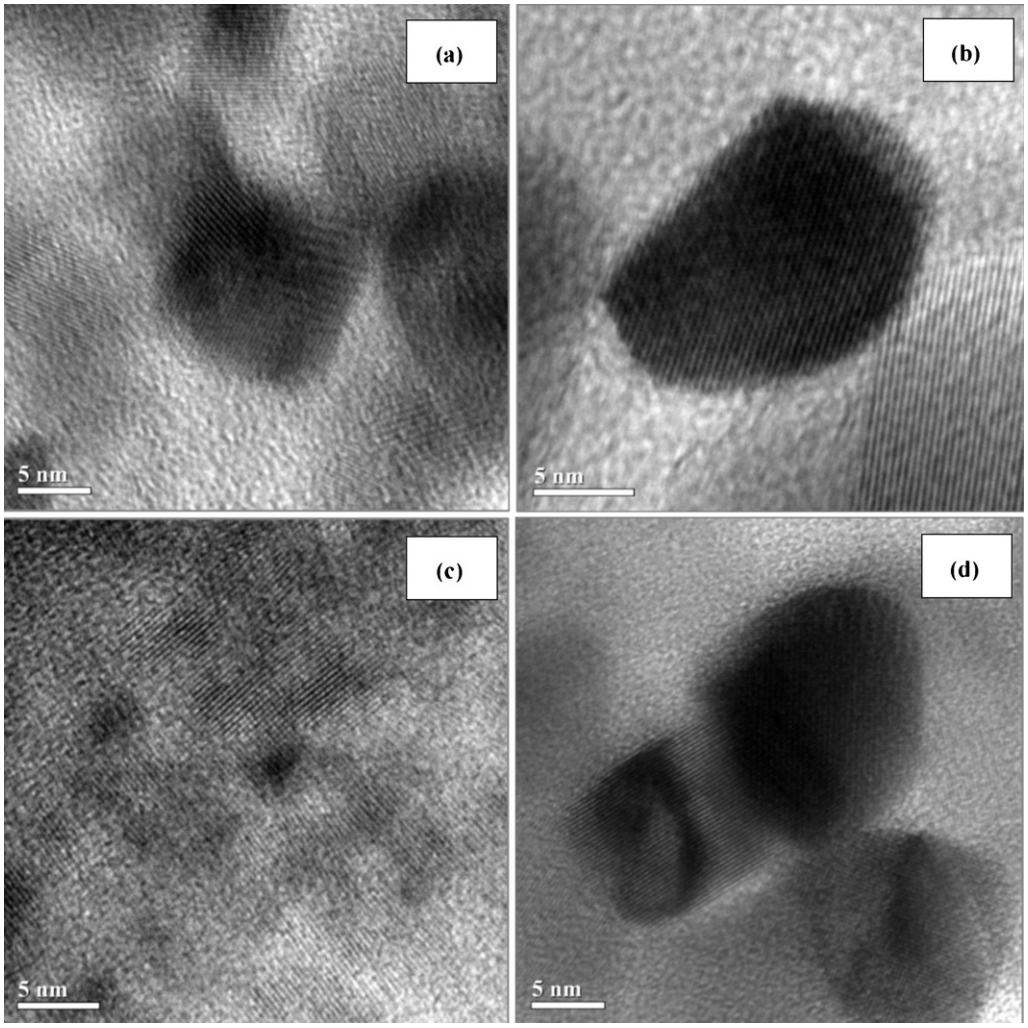

Fig. 7. High magnification TEM images of (a) synthesized mesoporous-assembled TiO_2 calcined at 500 °C, and commercial TiO_2 (b) P-25 TiO_2 (c) ST-01 TiO_2, and (d) JRC-03 TiO_2.

and degradation rates are observed when the photocatalyst dosage is increased up to 7 g/l. However, when it exceeds 7 g/l, the photocatalytic rate constants adversely decrease. The photocatalytic decolorization and degradation rates at this optimum photocatalyst dosage value of 7 g/l of the mesoporous-assembled TiO_2 nanoparticle were 1.07 and 0.68 h^{-1}, respectively. On the basis of the relevant band gap absorption of the investigated photocatalyst dosage, the results can be explained in terms of the availability of surface active sites on the TiO_2 photocatalyst, the light absorption of the photocatalyst, and the light penetration capability into the suspension [12]. With increasing the photocatalyst dosage until reaching the optimum value, the TiO_2 surface active sites, as well as the absorption ability of the TiO_2, accordingly increased. On the other hand, under a higher photocatalyst dosage, there was still only a small portion of the TiO_2 particles near the photocatalytic reactor wall that can completely absorb the incident light. This means that at a very high photocatalyst dosage, the photocatalyst has high tendency to be agglomerated, resulting in lowering the surface exposure to the light irradiation. Furthermore, the light penetration depths from the photocatalytic reactor wall become less due to the agglomeration and sedimentation of particles under a higher photocatalyst dosage, which could result in the light scattering, thus dramatically reducing the intensity of light entering the irradiated suspension [18].

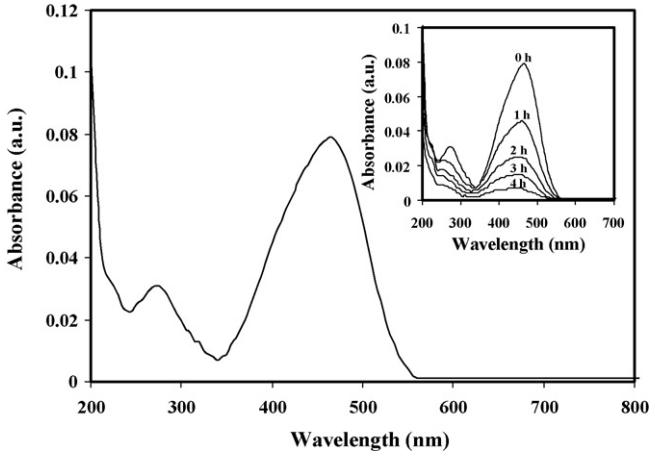

Fig. 8. UV–vis absorption spectrum of MO solution (Inset: UV–vis absorption spectra change upon irradiation time using the synthesized mesoporous-assembled TiO_2 photocatalyst calcined at 500 °C; photocatalyst dosage = 2 g/l; initial MO concentration = 5 mg/l; reaction volume = 80 ml).

3.2.3. *Effect of initial MO concentration*

From literature, the dye degradation rate increases with increasing dye concentration up to a particular level, and a further increase in dye concentration brings about the decrease the dye degradation

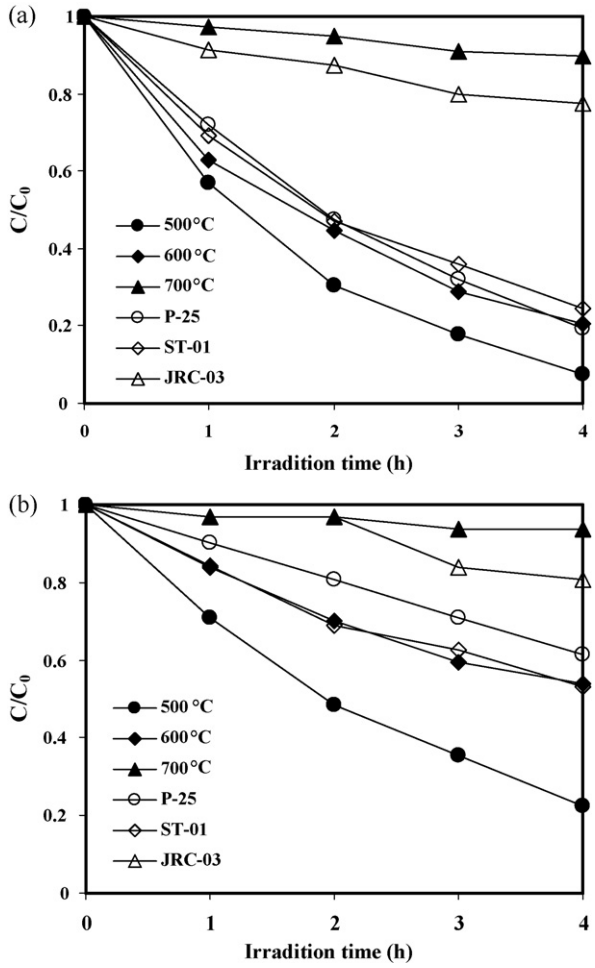

Fig. 9. Effect of photocatalyst type on the relative concentration (C/C_0) for (a) decolorization and (b) degradation of MO by the synthesized mesoporous-assembled TiO_2 photocatalysts calcined at various temperatures (500, 600, and 700 °C) and commercial TiO_2 photocatalysts as a function of irradiation time (photocatalyst dosage = 2 g/l; initial MO concentration = 5 mg/l; reaction volume = 80 ml).

rate. The reaction rate constants for the photocatalytic decolorization and degradation of MO at various initial MO concentrations using the synthesized mesoporous-assembled TiO_2 calcined at 500 °C are depicted in Fig. 11. The degradation rates (both decolorization and degradation) of MO increase with increasing initial

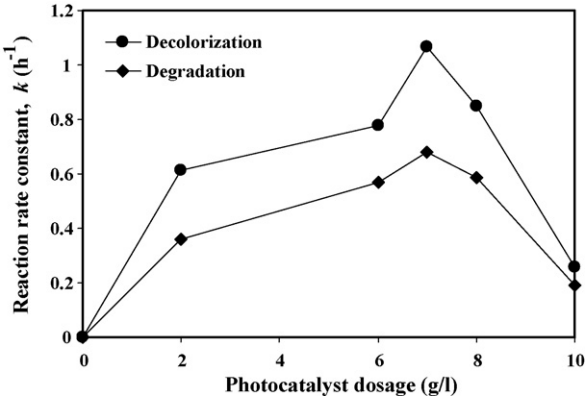

Fig. 10. Effect of photocatalyst dosage on the reaction rate constants for both decolorization and degradation of MO by the synthesized mesoporous-assembled TiO_2 photocatalyst calcined at 500 °C (initial MO concentration = 5 mg/l; reaction volume = 80 ml; irradiation time = 4 h).

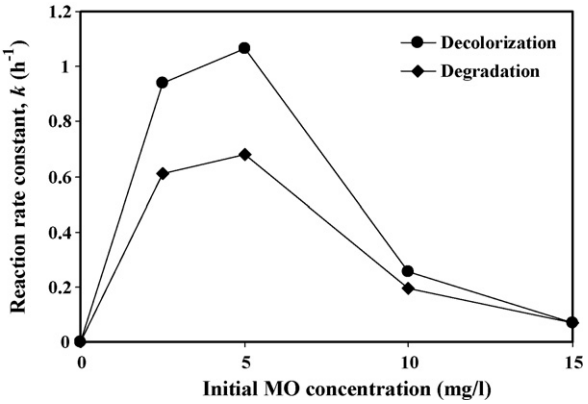

Fig. 11. Effect of initial MO concentration on the reaction rate constants for both decolorization and degradation of MO by the synthesized mesoporous-assembled TiO_2 photocatalyst calcined at 500 °C (photocatalyst dosage = 7 g/l; reaction volume = 80 ml; irradiation time = 4 h).

MO concentration up to 5 mg/l and then decrease with further increasing initial MO concentration from 5 to 15 mg/l. It can be explained in that the degradation rate strongly relates to the formation probability of the oxygen active radicals, i.e. $OH^{\bullet}$ and $O_2^{\bullet -}$, on the photocatalyst surface and also significantly relates to the probability of the $OH^{\bullet}$ and $O_2^{\bullet -}$ radicals to react with the MO dye molecules [12]. When the initial MO concentration increases, the reaction probability between the MO dye molecules and the oxygen active species also increases, consequently resulting in an enhancement in the decolorization and degradation rates. However, the MO degradation efficiency decreases as the initial MO concentration further increases. The possible reason may be because at high initial MO concentrations, the formation of the active oxygen radicals on the photocatalyst surface is decreased since the active sites are covered more by the MO dye ions. Another possible reason is the significant absorption of light by the MO dye itself present in the solution and/or on the photocatalyst surface instead of that by the photocatalyst in the same light wavelength range, and this therefore diminishes the overall efficiency of the photocatalytic reaction because the concentrations of the oxygen active species decrease [12]. Moreover, this decreasing tendency can be related to the formation of several layers of adsorbed dyes on the photocatalyst surface, being higher at higher dye concentrations [53]. The large amount of the adsorbed dyes can decrease the reaction probability between the dye molecules and the photoinduced valence band holes/oxygen radicals and subsequently decrease the amount of the aforementioned generated oxygen active species, reasonably due to the increased distance between the reactant molecules and the photocatalyst surface. Therefore, it can be concluded that the suitable initial MO concentration for the photocatalytic reaction of the mesoporous-assembled TiO_2 calcined at 500 °C with 7 g/l photocatalyst dosage was 5 mg/l.

3.2.4. Effect of H_2O_2 concentration

In order to increase the photocatalytic degradation rate of the MO dye by the synthesized mesoporous-assembled TiO_2 nanoparticle calcined at 500 °C, H_2O_2, which is a strong oxidant, was added to the reaction suspension. Fig. 12 shows the reaction rate constant for the photocatalytic decolorization of MO by the synthesized mesoporous-assembled TiO_2 at various H_2O_2 concentrations. It is worth noting that for the effect of H_2O_2 concentration, only the decolorization of MO due to the decrease in the absorbance peak centered at 465 nm could be determined and reported, not for its degradation. It has been observed that the absorbance peak centered at 270 nm is significantly interfered by

the added H_2O_2, the degradation of aromatic part of MO could not be examined in this study. Moreover, the photodegradation of MO in the system containing the photocatalyst and a 0.5 M H_2O_2 (optimum value as shown later) without the light irradiation did not occur, whereas the decolorization rate constant of MO at a 0.5 M H_2O_2 with the light irradiation and without the photocatalyst (homogeneous system) was observed to be only 0.15 h^{-1}.

From Fig. 12, when the H_2O_2 concentration is increased up to 0.5 M, the decolorization rate greatly increases. The gradual decrease in the decolorization rate is observed when further increasing H_2O_2 concentration from 0.5 to 0.9 M. The improved photocatalytic activity of the mesoporous-assembled TiO_2 photocatalyst in the presence of H_2O_2 with the concentration up to 0.5 M is attributed to the increased reactive hydroxyl radical intermediate ($OH^•$) formed from the reaction between the H_2O_2 oxidant and the photogenerated conduction band electrons. The H_2O_2 can exert a dual function: as a strong oxidant itself and as an electron scavenger, thus inhibiting the undesired electron-hole recombination at both the photocatalyst surface and bulk [54]. On the other hand, the photocatalytic decolorization rate decreases with further increasing H_2O_2 concentration to be higher than 0.5 M, plausibly due to too high quantity of the reactive $OH^•$ radicals. The radical–radical recombination as an undesired competitive reaction must be taken into consideration. In addition, if a high amount of H_2O_2 adsorbs onto the TiO_2 particle surface, the photocatalytic decolorization rate would be subsequently decreased due to the light screening effect of the H_2O_2 itself, causing less photoexcitation of the photocatalyst [55].

3.2.5. Effect of initial solution pH

The pH of solution is an important parameter affecting the photocatalytic reactions since it influences the surface charge properties of the TiO_2, the size of aggregates formed, the charge of the dye molecules, the adsorption of MO dye onto the TiO_2 surface, and the concentration of the hydroxyl radicals. In this work, both HCl and NaOH were used to adjust the MO solution pH in the range of 3–8. Fig. 13 shows the reaction rate constant for the photocatalytic decolorization of MO over the synthesized mesoporous-assembled TiO_2 calcined at 500 °C at various solution pHs in the presence of a 0.5 M H_2O_2. It is also worth noting that the decolorization of MO was only reported due to the interference of pH-adjusting compounds on the low wavelength absorption band.

As seen in Fig. 13, the higher photocatalytic decolorization occurs at the solution pH lower than the point of zero charge

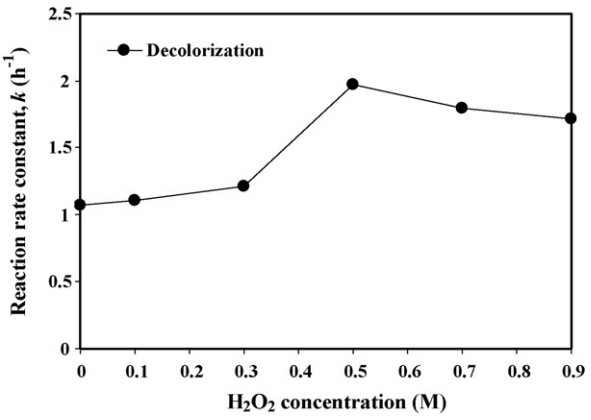

Fig. 12. Effect of H_2O_2 concentration on the reaction rate constant for decolorization of MO by the synthesized mesoporous-assembled TiO_2 photocatalyst calcined at 500 °C (initial MO concentration = 5 mg/l; photocatalyst dosage = 7 g/l; reaction volume = 80 ml; irradiation time = 4 h).

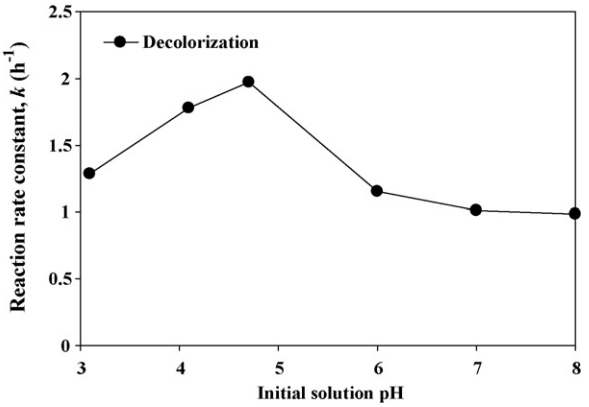

Fig. 13. Effect of initial solution pH on the reaction rate constant for decolorization of MO by the synthesized mesoporous-assembled TiO_2 photocatalyst calcined at 500 °C (initial MO concentration = 5 mg/l; photocatalyst dosage = 7 g/l; H_2O_2 concentration = 0.5 M; reaction volume = 80 ml; irradiation time = 4 h).

(pzc) of TiO_2, which is approximately 6.0 ± 0.3 [56]. When MO is dissolved in water, its structure becomes negatively charged. In contrast, the surface of the TiO_2 photocatalyst becomes positively charged when the solution pH is lower than its pzc. These opposite charges between the dissolved MO and the TiO_2 particles favorably lead to enhancing the photocatalytic decolorization rate due to the increase in their induced interaction. The optimum pH value for this photocatalytic reaction system was found at the solution pH of 4.7, which is lower than the pzc of TiO_2. In addition, the increased decolorization rate at this acidic pH can be possibly explained on the basis that at this low pH, $HO_2^•$ radical is also able to form, and this can compensate with the decrease in the generated $OH^•$ radical concentration [54]. However, at the lower pHs of 4.1 and 3.1, the photocatalytic decolorization rate decreases due to the possible agglomeration of the TiO_2 particles, which consequently reduces the total surface area available for the reactant adsorption and the photon absorption. Moreover, at too low pH with the excess concentration of H^+, the H^+ ions can interact with the azo link (–N=N–), which can be particularly subject to be the electrophilic attack by the hydroxyl radicals, leading to decreasing the electron densities at the azo group. Consequently, the reactivity of the hydroxyl radicals by the electrophilic mechanism decreases [55]. At the alkali solution pHs of 7.0 and 8.0, the photocatalytic decolorization rate decreases remarkably with increasing solution pH. Under these conditions, there is a Coulombic repulsion between the negatively charged surface of the photocatalyst and the negatively charged MO molecules, and the decreased interaction due to the aforementioned repulsion can limit the diffusion of the surface-generated $OH^•$ radicals towards the MO anions for the subsequent reaction [12,53]. Therefore, the photocatalytic decolorization process would be unavoidably lowered.

Subsequent to the optimization of all the investigated reaction parameters, a qualitative analysis of the MO degradation efficiency was determined by a TOC analyzer using the optimum conditions (photocatalyst dosage = 7 g/l; initial MO concentration = 5 mg/l; H_2O_2 concentration = 0.5 M; and initial solution pH = 4.7) over the best photocatalyst in this work, i.e. the synthesized mesoporous-assembled TiO_2 photocatalyst calcined at 500 °C. The TOC result revealed that the organic content could be greatly degraded up to approximately 85% at an irradiation time of 4 h. This suggests that the synthesized photocatalyst calcined at the suitable condition can be efficiently applied for the photocatalytic degradation of azo dye-containing wastewaters due to its high efficiency for both color and organic removal.

4. Conclusions

In this work, the synthesized mesoporous-assembled TiO_2 nanoparticle photocatalyst was synthesized by the sol-gel process with the aid of structure-directing surfactant and used for investigating the photocatalytic degradation of MO, as compared to commercially available non-mesoporous-assembled TiO_2 powders. Various synthetic and reaction parameters, including photocatalyst type, calcination condition for the photocatalyst preparation, photocatalyst dosage, initial MO concentration, H_2O_2 concentration, and initial solution pH, were studied on the photocatalytic MO degradation performance. Among all the investigated TiO_2 photocatalysts, the mesoporous-assembled TiO_2 calcined at a suitable temperature of 500 °C exhibited the superior performance for the MO degradation to the non-mesoporous-assembled commercial TiO_2. The optimum conditions for the photocatalytic MO degradation using such the mesoporous-assembled TiO_2 were obtained as follows: a photocatalyst dosage of 7 g/l, an initial MO concentration of 5 mg/l, a H_2O_2 concentration of 0.5 M, and an initial solution pH of 4.7, providing the highest photocatalytic MO degradation.

Acknowledgments

This work was supported by the Asahi Glass Foundation, Japan, the Sustainable Petroleum and Petrochemicals Research Unit, Center for Petroleum, Petrochemicals, and Advanced Materials, Chulalongkorn University, Thailand, and the Applied Surfactants for Separation and Pollution Control Research Unit under the Ratchadapisek Somphot Endowment Fund, Chulalongkorn University, Thailand. The authors would also like to express sincere gratitude to Prof. Susumu Yoshikawa, Institute of Advanced Energy, Kyoto University, Japan, for his invaluable advice.

References

[1] F.P. van der Zee, S. Villaverde, Water Res. 39 (2005) 1425–1440.
[2] Y. Liu, X. Chen, J. Li, C. Burda, Chemosphere 61 (2005) 11–18.
[3] M.R. Hoffmann, S.T. Martin, W. Choi, D.W. Bahnemann, Chem. Rev. 95 (1995) 69–96.
[4] O. Carp, C.L. Huisman, A. Reller, Prog. Solid State Chem. 32 (2004) 33–177.
[5] D. Chatterjee, S. Dasgupta, J. Photochem. Photobiol. C: Photochem. Rev. 6 (2005) 186–205.
[6] T. Robinson, G. McMullan, R. Marchant, P. Nigam, Biores. Technol. 77 (2001) 247–255.
[7] Y. Fu, T. Viraraghavan, Biores. Technol. 79 (2001) 251–262.
[8] E. Forgacs, T. Cserhati, G. Oros, Environ. Int. 30 (2004) 953–971.
[9] G. Crini, Biores. Technol. 97 (2006) 1061–1085.
[10] A.B. dos Santos, F.J. Cervantes, J.B. van Lier, Biores. Technol. 98 (2007) 2369–2385.
[11] H. Lachheb, E. Puzenat, A. Houas, M. Ksibi, E. Elimame, C. Guillard, J.M. Herrmann, Appl. Catal. B: Environ. 39 (2002) 75–90.
[12] I.K. Konstantinou, T.A. Albanis, Appl. Catal. B: Environ. 49 (2004) 1–14.
[13] D.F. Ollis, E. Pelizzetti, N. Serpone, Environ. Sci. Technol. 25 (1991) 1523–1529.
[14] M.A. Fox, M.T. Dulay, Chem. Rev. 83 (1995) 341–357.
[15] A. Fujishima, X. Zhang, D.A. Tryk, Int. J. Hydrogen Energy 32 (2007) 2664–2672.
[16] A. Houas, H. Lachheb, M. Ksibi, E. Elaloui, C. Guillard, J.M. Herrmann, Appl. Catal. B: Environ. 31 (2001) 145–157.
[17] M. Vautier, C. Guillard, J.M. Hermann, J. Catal. 201 (2001) 46–59.
[18] C.M. So, M.Y. Cheng, J.C. Yu, P.K. Wong, Chemosphere 46 (2002) 905–912.
[19] R.K. Wahi, Y. Liu, J.C. Falkner, V.L. Colvin, J. Colloid Interf. Sci. 302 (2006) 530–536.
[20] I. Oja, A. Mere, M. Krunks, R. Nisumaa, C.H. Solterbeck, M. Es-Souni, Thin Solid Films 515 (2006) 674–677.
[21] H.H. Ou, S.L. Lo, Sep. Purif. Technol. 58 (2007) 179–191.
[22] E. Alonso, I. Montequi, S. Lucas, M.J. Cocero, J. Supercrit. Fluid 39 (2007) 453–461.
[23] S.J. Doh, C. Kim, S.G. Lee, S.J. Lee, H. Kim, J. Hazard. Mater. 154 (2008) 118–127.
[24] M.R. Mohammadi, D.J. Fray, A. Mohammadi, Micropor. Mesopor. Mater. 112 (2008) 392–402.
[25] Z. Zhang, C.C. Wang, R. Zakaria, J.Y. Ying, J. Phys. Chem. B 102 (1998) 10871–10878.
[26] V.A. Sakkas, I.M. Arabatzis, I.K. Konstantinou, A.D. Dimou, T.A. Albanis, P. Falaras, Appl. Catal. B: Environ. 49 (2004) 195–205.
[27] V.F. Stone Jr., R.J. Davis, Chem. Mater. 10 (1998) 1468–1474.
[28] S. Kambe, K. Murakoshi, T. Kitamura, Y. Wada, S. Yanagida, H. Kominami, Y. Kera, Sol. Energy Mater. Sol. C 61 (2000) 427–441.
[29] K.M.S. Khalil, M.I. Zaki, Powder Technol. 120 (2001) 256–263.
[30] L. Kavan, J. Rathouský, M. Grätzel, V. Shklover, A. Zukal, Micropor. Mesopor. Mater. 44–45 (2001) 653–659.
[31] J.C. Yu, J. Yu, L. Zhang, W. Ho, J. Photochem. Photobiol. A: Chem. 148 (2002) 263–271.
[32] Q. Dai, L.Y. Shi, Y.G. Luo, J.L. Blin, D.J. Li, C.W. Yuan, B.L. Su, J. Photochem. Photobiol. A: Chem. 148 (2002) 295–301.
[33] N. Phonthammachai, T. Chairassameewong, E. Gulari, A.M. Jamieson, S. Wongkasemjit, Micropor. Mesopor. Mater. 66 (2003) 261–271.
[34] J. Du, Z. Liu, Z. Li, B. Han, Y. Huang, Y. Gao, Micropor. Mesopor. Mater. 83 (2004) 19–24.
[35] K.S. Yoo, T.G. Lee, J. Kim, Micropor. Mesopor. Mater. 84 (2005) 211–217.
[36] S. Miao, Z. Miao, Z. Liu, B. Han, H. Zhang, J. Zhang, Micropor. Mesopor. Mater. 95 (2006) 26–30.
[37] D.L. Shieh, J.S. Li, M.J. Shieh, J.L. Lin, Micropor. Mesopor. Mater. 98 (2007) 339–343.
[38] S. Yuan, Q. Sheng, J. Zhang, H. Yamashita, D. He, Micropor. Mesopor. Mater. 110 (2008) 501–507.
[39] T. Sreethawong, Y. Suzuki, S. Yoshikawa, J. Solid State Chem. 178 (2005) 329–338.
[40] T. Sreethawong, Y. Suzuki, S. Yoshikawa, Int. J. Hydrogen Energy 30 (2005) 1053–1062.
[41] T. Sreethawong, S. Yoshikawa, Catal. Commun. 6 (2005) 661–668.
[42] T. Sreethawong, S. Yoshikawa, Int. J. Hydrogen Energy 31 (2006) 786–796.
[43] B.D. Cullity, Elements of X-ray Diffraction, Addison-Wesley Pub. Co, Reading, MA, 1978.
[44] A.K. Gupta, A. Pal, C. Sahoo, Dyes Pigments 69 (2006) 224–232.
[45] T. Puangpetch, T. Sreethawong, S. Yoshikawa, S. Chavadej, J. Mol. Catal. A: Chem. 287 (2008) 70–79.
[46] A.O. Ibhadon, G.M. Greenway, Y. Yue, P. Falaras, D. Tsoukleris, Appl. Catal. B: Environ. 84 (2008) 351–355.
[47] F. Rouquerol, J. Rouquerol, K. Sing, Adsorption by Powders and Porous Solids: Principles, Methodology and Applications, Academic Press, San Diego, 1999.
[48] J.V. Smith, X-ray Powder Data File, American Society for Testing Materials, New York, 1960.
[49] R.A. Spurr, H. Myers, Anal. Chem. 29 (1957) 760–762.
[50] A. Fuerte, M.D. Hernandez-Alonso, A.J. Maire, A. Martinez-Arias, M. Fernadez-Garcia, J.C. Conesa, G. Munuera, J. Catal. 212 (2002) 1–9.
[51] K. Selvam, M. Muruganandham, M. Swaminathan, Sol. Energy Mater. Sol. C 89 (2005) 61–74.
[52] C. Hachem, F. Bocquillon, O. Zahraa, M. Bouchy, Dyes Pigments 49 (2001) 117–125.
[53] W.F. Yao, X.H. Xu, H. Wang, J.T. Zhou, X.N. Yang, Y. Zhang, S.X. Shang, B.B. Huang, Appl. Catal. B: Environ. 52 (2004) 109–116.
[54] C.K. Grätzel, M. Jirousek, M. Grätzel, J. Mol. Catal. 60 (1990) 375–387.
[55] J. Sun, L. Qiao, S. Sun, G. Wang, J. Hazard. Mater. 155 (2008) 312–319.
[56] G.A. Parks, Chem. Rev. 65 (1965) 177–198.